Microfluidic platform using focused ultrasound passing through hydrophobic meshes with jump availability

Yusuke Koroyasu [ID][a,b], Thanh-Vinh Nguyen[c], Shun Sasaguri[a], Asier Marzo [ID][d], Iñigo Ezcurdia [ID][d], Yuuya Nagata [ID][e], Tatsuya Yamamoto[f], Nobuhiko Nomura[f,g,h], Takayuki Hoshi [ID][i], Yoichi Ochiai [ID][i,j,k] and Tatsuki Fushimi [ID][j,k,*]

[a]School of Informatics, College of Media Arts, Science and Technology, University of Tsukuba, Tsukuba, 305-8550 Ibaraki, Japan
[b]Graduate School of Comprehensive Human Sciences, University of Tsukuba, Tsukuba, 305-8550 Ibaraki, Japan
[c]Sensing System Research Center, National Institute of Advanced Industrial Science and Technology (AIST), Tsukuba, 305-8564 Ibaraki, Japan
[d]UPNALab, Department of Mathematics and Computer Engineering, Public University of Navarra, Pamplona, 31006 Navarra, Spain
[e]Institute for Chemical Reaction Design and Discovery, Hokkaido University, Sapporo, 001-0021 Hokkaido, Japan
[f]Faculty of Life and Environmental Sciences, University of Tsukuba, Tsukuba, 305-8577 Ibaraki, Japan
[g]Microbiology Research Center for Sustainability, University of Tsukuba, Tsukuba, 305-8577 Ibaraki, Japan
[h]Life Science Center for Survival Dynamics, Tsukuba Advanced Research Alliance, University of Tsukuba, Tsukuba, 305-8577 Ibaraki, Japan
[i]Pixie Dust Technologies, Inc., Chiyoda-ku, 101-0061 Tokyo, Japan
[j]R&D Center for Digital Nature, University of Tsukuba, Tsukuba, 305-8550 Ibaraki, Japan
[k]Institute of Library, Information and Media Science, University of Tsukuba, Tsukuba, 305-8550 Ibaraki, Japan
*To whom correspondence should be addressed: Email: tfushimi@slis.tsukuba.ac.jp
Edited By: E. Kanso

Abstract

Applications in chemistry, biology, medicine, and engineering require the large-scale manipulation of a wide range of chemicals, samples, and specimens. To achieve maximum efficiency, parallel control of microlitre droplets using automated techniques is essential. Electrowetting-on-dielectric (EWOD), which manipulates droplets using the imbalance of wetting on a substrate, is the most widely employed method. However, EWOD is limited in its capability to make droplets detach from the substrate (jumping), which hinders throughput and device integration. Here, we propose a novel microfluidic system based on focused ultrasound passing through a hydrophobic mesh with droplets resting on top. A phased array dynamically creates foci to manipulate droplets of up to 300 μL. This platform offers a jump height of up to 10 cm, a 27-fold improvement over conventional EWOD systems. In addition, droplets can be merged or split by pushing them against a hydrophobic knife. We demonstrate Suzuki-Miyaura cross-coupling using our platform, showing its potential for a wide range of chemical experiments. Biofouling in our system was lower than in conventional EWOD, demonstrating its high suitability for biological experiments. Focused ultrasound allows the manipulation of both solid and liquid targets. Our platform provides a foundation for the advancement of micro-robotics, additive manufacturing, and laboratory automation.

Keywords: microfluidics, ultrasound, hydrophobic, automation

Significance Statement

Our droplet-based platform using focused ultrasound represents a novel approach in microfluidics. The platform manipulates targets (both liquids and solids) on a hydrophobic mesh. It supports droplet volumes up to 300 μL and provides manipulation of up to four droplets simultaneously. Jump heights of up to 10 cm can be achieved, a 27-fold increase over conventional electrowetting-on-dielectric systems. Focused ultrasound offers jumping functionality, low biofouling, and potential for chemical experiments, making it suitable for automation, micro-robotics, or additive manufacturing. The platform provides a foundation for future advancements in the field of microfluidics and a new perspective on the use of focused ultrasound technology.

Introduction

Microfluidics consists in the manipulation of small volumes of liquids, typically from picoliters to microliters. It is becoming ubiquitous in science and engineering (1, 3, 4, 2) to automate and improve the throughput of experiments involving droplets. Consequently, a wide range of digital microfluidic (DMF)

platforms has been developed (4, 8, 1, 5, 9, 6, 7). The most common DMF technique is electrowetting on dielectric (EWOD), which manipulates droplets using an imbalance of forces induced by the spatially varying wetting properties of a substrate. In general, these platforms manipulate droplets on top of a 2D surface. In recent years, jumping from the substrate has been

developed to improve throughput for analysis and device integration ([13], [11], [12], [10]).

However, despite significant research in this area, the achievable jump height is limited to less than 5 mm and require complex electrode geometries, limiting the deployment of EWOD-based techniques. Other approaches have been developed, such as pyroelectric ([15], [14]) and photovoltaic ([16]) droplet manipulations. The pyroelectric effect uses laser heating to control the surface charge density (SCD) so that the droplet is moved by dielectrophoretic force. SCD can also be controlled by the photovoltaic effect to manipulate droplets using the electrophoretic force. Because these methods do not rely on droplet deformation, they enable jumps of up to 16 (1.4 μL) and 50 (0.6 μL) mm, respectively.

In this study, we proposed a microfluidic device with large jump capabilities based on focused ultrasound (Fig. 1A). A focused ultrasound beam is generated by a phased array of transducers (PATs) and passes through an acoustically transparent mesh with hydrophobic treatment (see Methods); liquid droplets on top of the mesh are manipulated by the foci. This acoustic method is a new alternative to DMF platforms based on optical manipulation ([18], [17], [15], [14], [16]).

Due to the hydrophobic treatment, the droplets rest on top of the mesh without permeating; yet, acoustic waves can pass through the mesh. The PAT generated foci (Fig. 1B), 10 mm above the target droplet (see Methods section). As shown in Fig. 1C, this produces a stable and convergent acoustic radiation force (ARF) at or near the focal point along the horizontal direction. The acoustic focal point position can be updated dynamically to move the droplets horizontally. A vertical ARF was also generated at the acoustic focal point (Fig. 1D). Detachment of the droplet from the surface during horizontal transportation can be prevented by lowering the acoustic pressure (Pa) (e.g. by lowering the voltage supplied to the PAT). When the droplet is required to jump above the surface, the acoustic pressure at the focal point gets increased until the focus creates an ARF higher than the critical value ($>F_g + F_a$, where F_g and F_a are the gravitational and adhesion forces, respectively). As the droplets rest on the mesh without sticking to the surface, propulsion of a relatively large droplet can be achieved using this approach, and multiple droplets can be manipulated with minimal force. The acoustic manipulation of liquid droplets has been studied in the field of acoustic levitation ([20], [19], [22], [21]); however, their applications are limited because the volume and number of droplets that can be handled simultaneously are significantly constrained. All droplets must be levitated constantly, which restricts the number of droplets (three droplets maximum) and their size (3 mm diameter). In our approach, the foci do not require energy to constantly levitate all droplets, and energy is used more effectively to just move the droplets. Using our platform, we demonstrate the fundamental operations for microfluidics: horizontal manipulation, jumping, merging, and splitting. This platform achieves unprecedented features: droplets of different volumes (15, 30, 45, 60 μL) translated along a 26 mm linear path in 1 s, manipulation of a large droplet 300 μL, simultaneous manipulation of four droplets, and a jumping height of 128 mm. This jumping height is two times higher than that for state-of-the-art photovoltaics, even when using a droplet that is 24 times larger (15 μL). This technique is independent of the target material, enabling the horizontal manipulation and jumping of solid spheres and droplets. In applications with densely packed droplets, the jumping functionality can enhance droplet manipulation efficiency, reduce cross-contamination, and increase automation by allowing direct substrate-to-substrate jumps. This eliminates the need for sequential transfers through intermediate

steps. Additionally, for multi-stage droplet-based reactors, jumping enables direct stage-to-stage movement, preventing droplet interactions and contamination. This leads to improved reaction efficiency, better process control, and advantages such as parallel reactions and adaptable design.

Results

Horizontal manipulation

The horizontal manipulation of a droplet on a hydrophobic mesh is achieved by controlling the focal position horizontally. In acoustic levitation, hollow traps such as twins, bottles, or vortex traps are often used to generate stable forces along the axis, allowing objects to be held in mid-air ([23]). However, our platform uses a mesh to support the droplet, eliminating the need for vertical force convergence and only requiring converging forces in the xy-plane (horizontal forces) within the plane of the mesh, as illustrated in Fig. 1C, the focused ultrasound generates an attractive force in that plane. The horizontal manipulation of the droplet is shown in Fig. 2 and Movie S1. The PAT phases were controlled such that $(x_f, y_f, z_f) = (-12.8 \cos(2\pi f t), 0, 115)$ mm, where f is the frequency in Hz, with $0 \leq t \leq \frac{1}{f}$ and was set to $(x_f, y_f, z_f) = (-12.8, 0, 115)$ mm after $t > 1/f$.

Fig. 2A shows the time lapse of a moving droplet (45 μL) and Fig. 2B and C show the horizontal trajectory of the droplets moving at two frequencies ($f = 1.0, 0.2$ Hz) with four volumes (15, 30, 45, and 60 μL) and an applied voltage on the PAT of 10 V (see Methods). As shown in Fig. 2B and C, the droplets mostly follow the specified trajectory, except for 60 μL, which has a large mass and is difficult to move at a high speed. Some overshoot and underdamped oscillations were observed at $t = 1/2f$ and $1/f$ in Fig. 2B for all droplets. Although underdamped oscillations were more prevalent during the movement (more in Fig. 2C than in B), the magnitude of the steady-state error was similar in both cases. These trajectory errors are non-negligible. However, a closed-loop controller can be implemented to control the droplet more accurately. Satellite droplets were not generated in the process of moving the droplets.

Solid objects can also be manipulated using focused ultrasound. Movie S2 shows the manipulation of nylon beads (MonotaRO Co., Ltd.; density 1, 140 kg m^{-3}) with radii of 1.5, 2.0, and 2.5 mm. The ability to move both objects, regardless of their properties (solids or liquids), is unique to acoustophoretics.

Focused ultrasound can manipulate small droplets of less than 60 μL (See Supplementary Material and Fig. S10 for tiny droplets) as well as droplets larger than a wavelength. As shown in Movie S3, the 300 μL puddle droplets were manipulated in a circular path with a radius of 20 mm for 5 s at an input voltage of 10 V. Such large droplet manipulation is extremely challenging with acoustic levitation.

The iterative back-propagation (IBP) method ([24]), which is frequently used in acoustic levitation, was used to generate multiple foci and handle multiple droplets simultaneously. IBP code is made available in data availability section. Movie S4 used the IBP method with an input voltage of 20 V to generate four foci at 90 degrees on a 20 mm circular path, and four 40 μL droplets were manipulated simultaneously using this method. Multiple droplets can be controlled simultaneously; however, if the droplets are positioned closer than 10 mm to each other, they merge (Movie S5).

Jumping from the mesh

The focused ultrasound beam applies a force along its traveling direction (Fig. 1D). When the ARF exceeds the critical value (i.e. ARF > sum of gravitational and adhesion forces, the voltage level
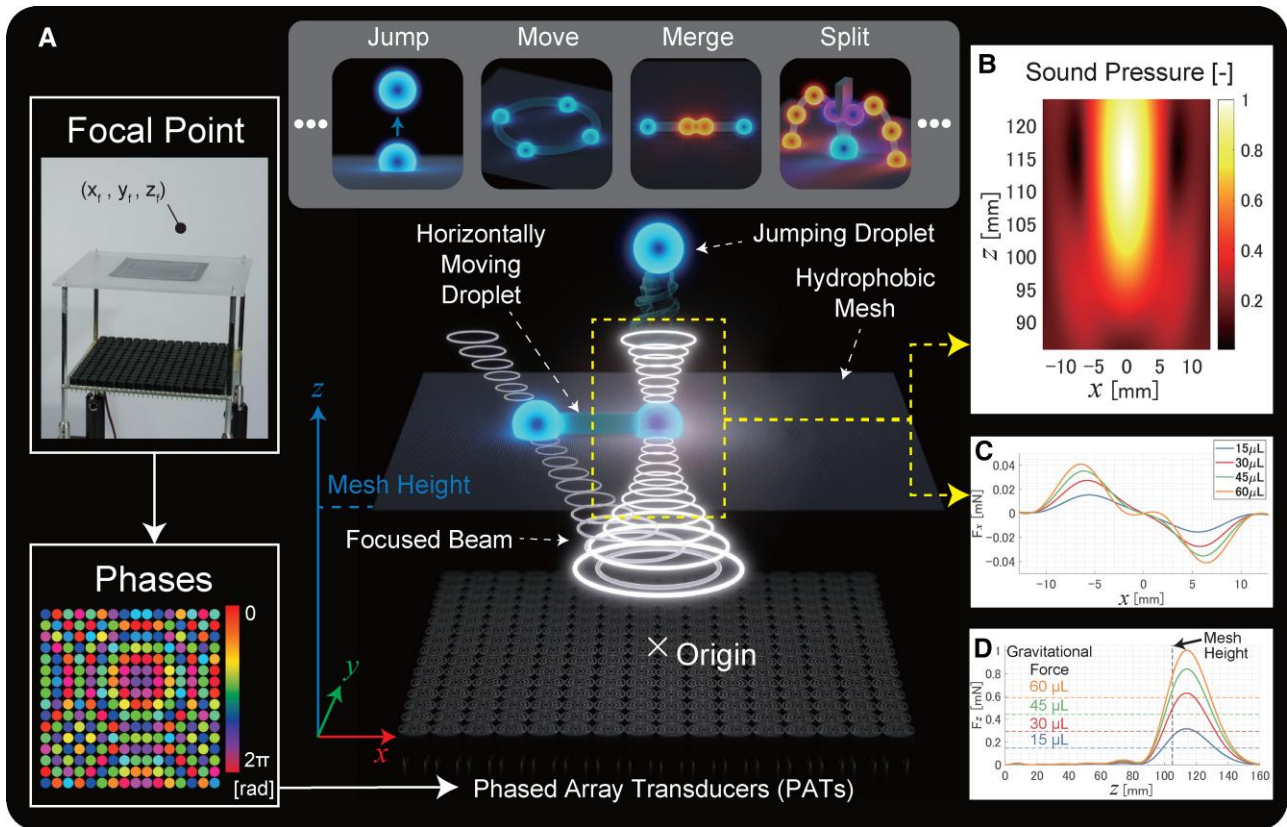
Fig. 1. Schematic of the system. A) The target focal position is defined, and the necessary emission phases are calculated for each transducer of the PAT. Due to the radiation force of the focused beam, the droplets jump, move, merge, or split. B) Simulated normalized sound pressure around the focal point (indicated by yellow dashed box in (A)) with focal point at $(x_f, y_f, z_f) = (0, 0, 115)$ mm. C,D) Simulated acoustic radiation force for 15, 30, 45, and 60 μL droplets along the x and z directions with the focal position at $(x_f, y_f, z_f) = (0, 0, 115)$ mm, and the mesh placed at z = 105 mm. The excitation voltage of the array in C is 10 V and in D is 16 V for horizontal movements and jumping, respectively.

at which the droplet detaches from the surface is provided in the supplementary material and Fig. S6), the droplet detaches from the surface and jumps in mid-air. Fig. 3 shows the detachment process of droplets from the mesh. The droplet initially rests on top of the mesh $((x, y, z) = (0, 0, 105)$ mm), and the focal point is aimed at $(x_f, y_f, z_f) = (0, 0, 115)$ mm for all cases in Fig. 3. We demonstrated the jumping of droplets with 15, 30, 45, and 60 μL (see Movie S6 and Methods for the experimental setup). The voltages applied to the transducers were 12 and 16 V. Sixty percent of the transducers were initially turned off to apply a lower amplitude and thus keep the droplet trapped. Detachment was then achieved by turning on all the transducers. The experiment was repeated five times. The jumping height is defined as the difference between the centroid of the droplet at the peak height and the beginning of the jump. When the applied voltage was 12 V, the average jumping height was 30.7 (SD = 0.78), 33.2 (SD = 1.87), 15.8 (SD = 4.23), and 3.25 mm (SD = 0.75) for 15, 30, 45, and 60 μL, respectively (Fig. 3A–D). Note that a 60 μL droplet failed to detach once.

When the applied voltage was increased to 16 V, the average jumping height increased to 108.8 (SD = 15.05), 78.0 (SD = 15.71), 59.7, 27.4 mm for 15, 30, 45, and 60 μL, respectively (Fig. 3E–H). A height of 108.8 mm are 27, 7, and 2 times greater than the jumping heights reported by the EWOD (12), pyroelectric (15), and photovoltaic (16) methods, respectively. The maximum recorded jumping height was 128.2 mm with a 15 μL droplet at 16 V. Large droplets could be detached, as shown in Fig. 3G and H. However, the droplet split into multiple droplets in the process; this occurred in three out of five attempts for 45 and 60 μL droplets.

The surface tension increases as the droplet radius exceeds the capillary length (2.3 mm in the case of water), and droplets above this radius easily break into small droplets owing to surface instability. Further engineering is required to make a large droplet jump without dispersion, for example, by applying a dynamic ease-in/ease-out in the amplitude of the focal point over time.

Although the experimental motion of the droplets and the numerical simulations were generally consistent, some discrepancies were observed. For example, when the numerical simulations predict that droplets will not jump, they jumped in the experiment (see Supplementary Material and Fig. S7). This may be because we assumed the droplet to be spherical in the simulation, but the droplet was not perfectly spherical owing to the wetting caused by the mesh and gravity. Therefore, the surface area impinged by the focal point is larger than that when the droplet is a perfect sphere, thereby increasing the force applied to the droplet. Movie S7 tests this hypothesis and compares the behavior of a solid sphere and a droplet with the same volume. When the applied voltage is 12 V, all solid spheres with a radius of 1.5, 2.0, and 2.5 mm do not jump as predicted through numerical simulation. Meanwhile, solids with a radius of 1.5, 2.0 and 2.5 mm jumped with 16 V, as the numerical simulation predicted (see Supplementary Material and Figs. S8 and S9).

Merging multiple droplets

Various droplets can be manipulated simultaneously by generating multiple focal points. Here, we generated two focal points
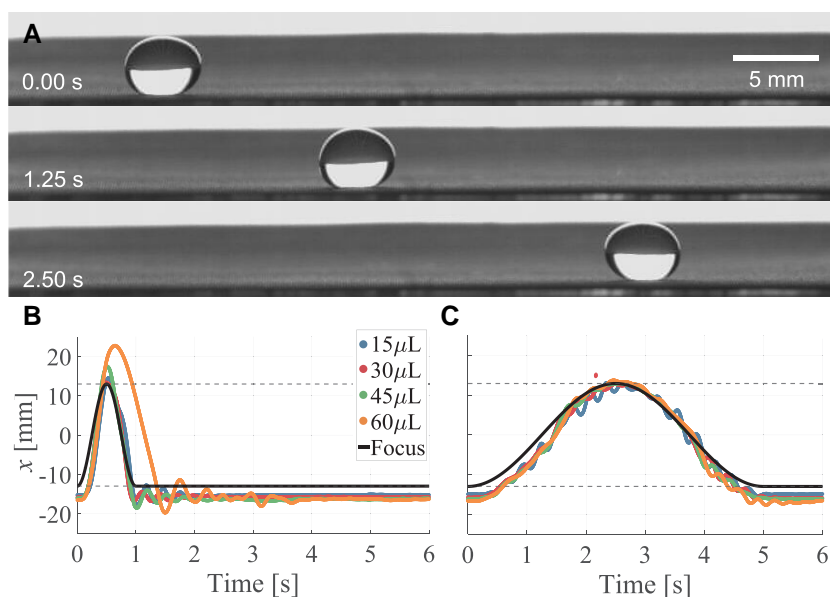
Fig. 2. Horizontal manipulation of a droplet (applied voltage is 10 V). A) Image series of a 45 μL droplet. The droplet was moved from left to right in the images for 25.6 mm (3.0λ) in 2.50 s. B) Tracked position of droplets of different volumes along with the focal point when they move at $f = 1.0$ and C) $f = 0.2$ Hz. See supplementary Movie S1.
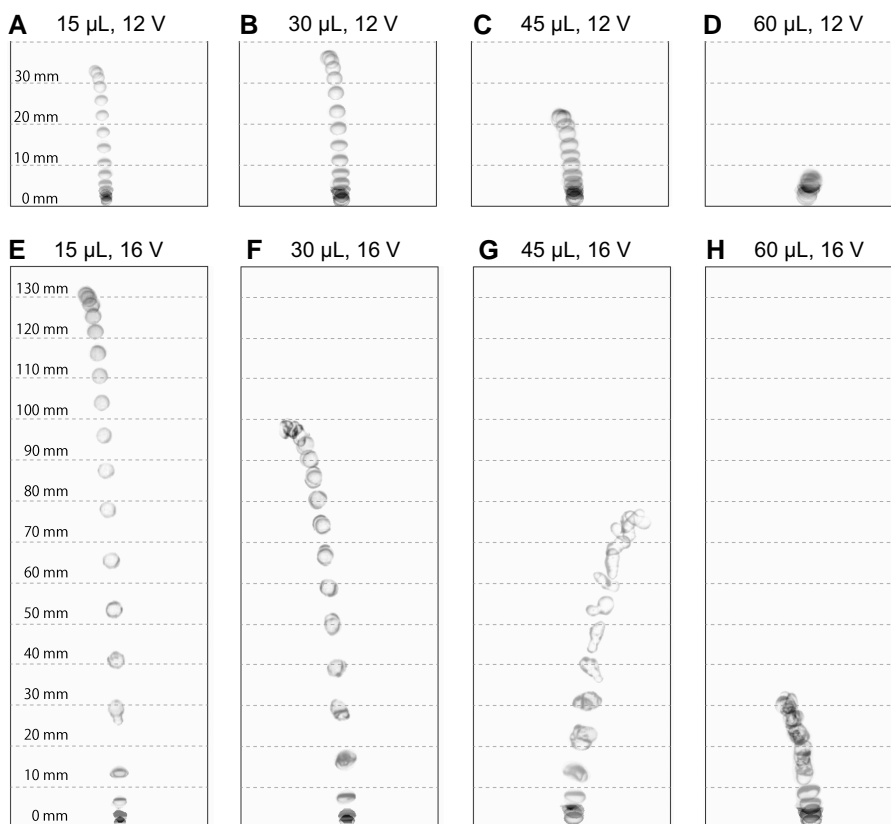

Fig. 3. Jumping of a droplet from the mesh with A,E) 15 μL, B,F 30 μL, C,G) 45 μL, and D,H) 60 μL. The applied voltage to the PAT was (A–D) 12 V and (E–H) 16 V. The sequence interval is 10 ms. The experiment was repeated five times. Notably, (D) only jumped once out of the five attempts because of its high mass and low supplied voltage. In (G–H), the droplet burst into multiple droplets in three out of five attempts. The video clip is provided in Movie S3.

using the method proposed by Andrade et al. (19), where half of the transducers were focused on droplet A and the other half on droplet B.

Fig. 4A shows the time lapse of merging process (30 μL) and Fig. 4B show the trajectory of the droplets at a supply voltage of 25 V. The focal points were initially placed at $(x_f, y_f, z_f) = (\pm 6.39\{1 + \cos(2\pi ft)\}, 0, kft + 115)$ mm, where $f = 0.4$ Hz $(0 \leq t \leq 1.25$ s). If the two focal points are translated horizontally (i.e. $k = 0$), the droplets jump and disperse as soon as they merge (Movie S8). Thus, the focal point was simultaneously shifted upward to avoid jumping after

coalescence. In Fig. 4, the value is set to $k = 20$. A suitable k value is different for each height and volume. If the gradient of the vertical shift is too high (e.g. when $k = 40$), the droplets fail to merge. Similarly, in Fig. 2B and C, each droplet approaches the center ($x = 0$) along the specified trajectory with some underdamped oscillations. The droplets then merged near the center at approximately 0.84 s. The oscillations are generated by merging decay, and the droplet stabilizes at the center.

While acoustic levitation can achieve merging in mid-air ([20], [19], [22]); it cannot continue to levitate the merged droplets if the combined size is larger than the half wavelength limit. Here, because the droplet rested on the mesh, it could be processed for further experiments and analysis.

Splitting

A hydrophobically treated knife was placed vertically 5 mm above the mesh, and a droplet of 45 μL was propelled into the knife with the PAT at 12 V (Fig. 5A). The experimental process was the same as that used for the jump experiment. The knife cuts the droplet in half at $t = 70$ ms, and the droplets continue to travel vertically and land on the mesh after free fall. 15 and 30 μL droplets could also be split (Movie S9). Whether the droplets can be successfully split is determined by the Weber number and the position where the droplet hits the knife ([25]). Further studies are necessary to split the droplets into accurate custom proportions.

Discussion

We demonstrated a microfluidics platform using focused ultrasound passing through a hydrophobic mesh that holds droplets on top. We showed the fundamental horizontal manipulation and jumping capabilities of the proposed device as well as operations such as merging and splitting. The maximum average jumping height achieved by the system was up to 10.9 cm. In the
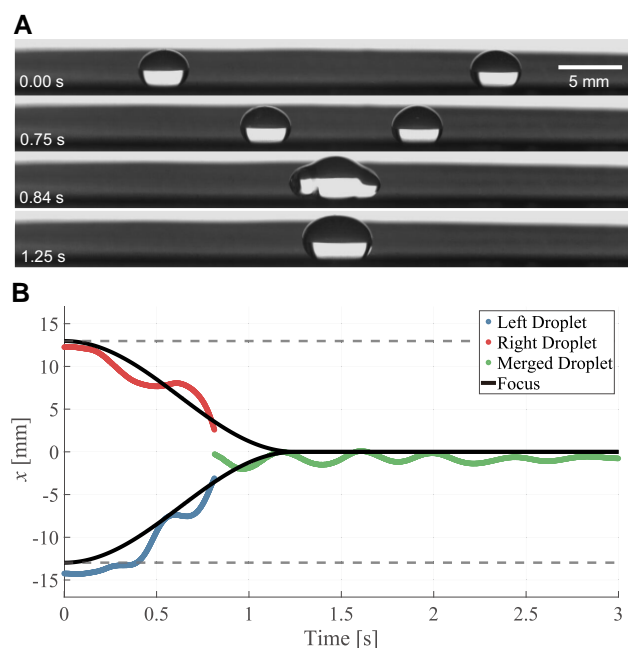

Fig. 4. Merging two droplets with a supplied voltage of 25 V. A) Two droplets were placed on the mesh at $(x, y, z) = (\pm 12.8, 0, 105)$ mm at $t = 0.0$ s, moved to the center, and merged at $t = 0.84$ s; eventually, the merged droplet becomes stable. B) Experimental results for the horizontal position of the two droplets when $k = 20$, along with the foci.

following section, we evaluate and discuss the current performance of our platform and the steps needed to excel in each field.

Chemical reaction

We performed the Suzuki-Miyaura cross-coupling, an essential carbon–carbon bond formation method in organic synthesis that is widely used in industry, to show its application in the chemical field. As shown in Fig. 5B and Movie S10, 20 μL droplets were dispensed on a hydrophobic tungsten mesh. To produce solution A, 1-(5-bromothiophen-2-yl)ethan-1-one (24 mM), N,N-dimethyl-4-(4,4,5,5-tetramethyl-1,3,2-dioxaborolan-2-yl)aniline (27 mM), and potassium carbonate (27 mM) were dissolved in dimethyl sulfoxide (DMSO; 50%) and water (50%) and filtered through a 0.45 μm polytetrafluoroethylene (PTFE) filter. To produce solution B, diacetoxypalladium (4.4 mM) was dissolved in acetone (10%) and water (90%). The two droplets were translated to the center (2.00 s) and merged (2.97 s). Under UV irradiation (375 nm), the merged droplets were almost colorless and transparent at first (3.67 s), but gradually fluoresced orange, indicating sufficient mixing and the presence of the Suzuki-Miyaura cross-coupling products (1-(5-(4-(dimethylamino)phenyl)thiophen-2-yl)ethan-1-one, 17.67 s) ([26]).

Because the applied acoustic force is independent of the material properties of the target, different compounds can be moved using focused ultrasound. System applicability is limited only when the liquid is not repelled by the mesh and sticks to or permeates it. We tested various chemicals that could be used in our current setup, which is currently limited to dimethylsulfoxide or aqueous solutions (see Supplementary Material and Fig. S11). Other chemicals, such as tetrahydrofuran and toluene, permeated through the mesh. Acetonitrile and N,N-dimethylformamide do not permeate, but stick to the surface. This limitation is bounded to our current hydrophobic mesh. Pan et al. ([27]) demonstrated a superomniphobic mesh coating method that can repel a wider range of chemicals, including N,N-dimethylformamide and toluene. In addition, the mesh used by Pan et al. was less dense than ours. Thus, employing it would result in a high-performance microfluidic platform in terms of the acoustic force that passes through the mesh and supported compounds.

Biocompatibility

DMF has been used for the automation of experiments with various bioanalytes. However, surface contamination through the adsorption of proteins, induced by the hydrophobicity of the device surface, is an issue that needs to be considered in current methods. It is known that protein adsorption reduces the hydrophobicity of the surface ([28]) and a system with adverse surface contamination becomes unusable (hydrophilic) over time. Thus, only samples with small concentrations (0.005 mg mL^{-1} fluorescein isothiocyanate-labeled bovine serum albumin (FITC-BSA) ([29])) of proteins can be moved on EWOD without the use of filler oil ([30]), Pluronic additives ([29]), or the application of specific pH and voltage biases ([31]). While we observed some protein adsorption on the hydrophobic mesh after exposure to the BSA droplets (Fig. S12); BSA droplet with concentrations of up to 1.0 mg mL^{-1} with buffer (10 mM tris–HCl pH 7.8) can be moved without the use of any additives.

This demonstrates that biofouling using our method is considerably lower than that EWOD methods. This is because the mesh has 42 percent openings, and unlike EWOD, a high voltage is not applied to the electrodes that are in contact with the samples ([14]). Thus, contamination is not problematic in practice as it is less affected by surface contamination, the working area of our platform is larger, meshes are inexpensive and replaceable, and droplets can
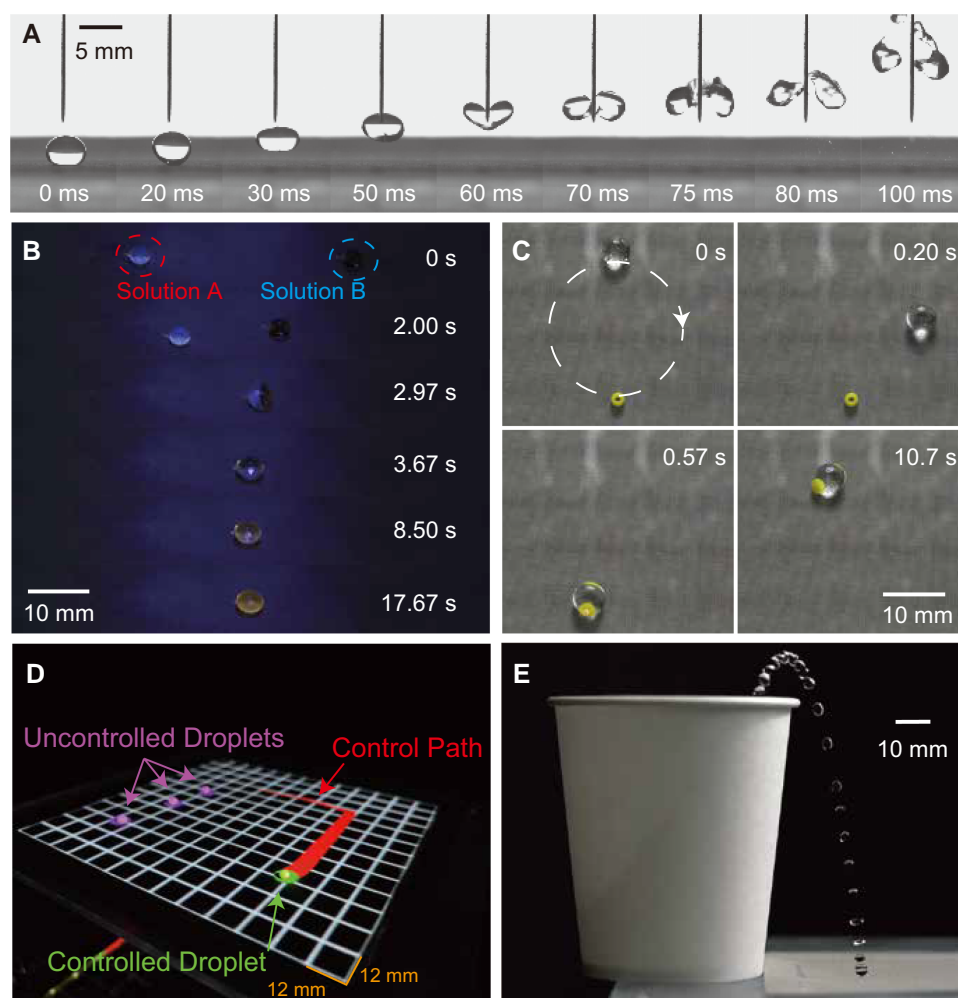
Fig. 5. Potential applications of our platform. A) Splitting of a liquid droplet (45 μL) by catapulting it into a hydrophobic knife placed 5 mm above the mesh. B) Suzuki-Miyaura cross-coupling (both 20 μL) is carried out on the mesh. After the two droplets were merged, orange emission was observed under UV irradiation. C) Residues can be cleaned up using a water droplet. D) Demonstration of augmented reality with images projected from a projector fixed above the mesh, 15 μL milk droplets were used to improve visibility. Selective manipulation of the droplets is possible, and non-manipulated droplets remain stationary. E) Droplet (15 μL, 17 V) jumping into a paper cup (height 80 mm).

easily jump between meshes, if necessary. Li et al. (14) successfully transported 20 mg mL^{-1} droplets in photopyroelectric microfluidics using a superomniphobic surface. Thus, our platform have the potential to reduce biofouling by applying this state-of-the-art surface treatment.

Surface cleaning

We demonstrated cleaning of the substrate surface by manipulating a water droplet (30 μL, 11 V) in Fig. 5C and Movie S11. The droplet was moved along a circular trajectory of radius 10 mm to collect a solid object (glass bead, TOHO Co., Ltd., density of 2500 kg m^{-3}, outer diameter 2.0 mm, height 1.4 mm, inside hole diameter 0.9 mm) in the trajectory (0.57 s). After collection, the droplets, and beads returned to their initial positions. This operation is required in experimental automation to clean the residues between trials. These beads are difficult to manipulate using acoustophoretic forces because of high friction between mesh and object. However, they can be easily transported by carrying them inside a water droplet.

Augmented reality application

In Fig. 5D and Movie S12, we demonstrate an augmented reality (AR) application that combines our microfluidic platform and projection

mapping. Users draw a path on a graphic interface, and the system applies the trajectory to the droplet. Simultaneously, the information regarding the path and position of the droplet was projected onto the mesh. This can improve human interaction with the systems when the experiments are not fully automatic and require human intervention. This system was created using TouchDesigner (Derivative, Inc.).

Jumping into a cup

The ability to propel droplets further than 10 cm enables a wider range of tasks. For example, Fig. 5E and Movie S13 show a water droplet (15 μL, 17 V) placed on $(x, y, z) = (-20, 0, 105)$ mm jumping diagonally into a cup (height = 80 mm). Applications in the food industry, additive manufacturing, and transferring droplets to other processor/analyzer/waste bins for experimental automation can be realized with the jumping capability.

Jump direction control

To demonstrate the controllability of the droplet jumping direction, we performed experiments using the same experimental setup shown in Fig. 3A droplet volume of 15 μL and an applied voltage of 14 V was used. The droplets motion was captured at 1,000 fps

with a resolution of 2, 048 × 2, 048 pixels using a high-speed camera (FASTCAM Nova R2, Photron). Initially, the focus was positioned at $(x_f, y_f, z_f) = (0, 0, 115)$ mm and 60% of the transducers were turned off to capture the droplet at the center of the grid. The x_f position was then shifted horizontally by $-\lambda/3, 0$, and $\lambda/3$, respectively, to induce the droplet to jump leftward, upward, and rightward, and all transducers were turned on. The experimental results showed that the trajectory of the droplet appeared as shown in Fig. S13. The leftward, upward, and rightward jumps are represented by blue, green, and red lines, respectively. The measured jump heights were 45.2, 52.3, and 40.3 mm (SD = 4.2, 2.7, and 7.4 mm), and the horizontal shifts were −19.8, −2.3, and 19.4 mm (SD = 4.7, 4.9, and 1.9 mm). To statistically compare the differences in landing positions between upward jumps and left/right jumps, one-tailed Wilcoxon rank-sum tests were performed at the 1% significance level. The P-values obtained were 0.000091 and 0.000091, respectively, rejecting the null hypothesis that the medians of the two populations are equal. This shows the ability to control the direction of droplet jumping by horizontally shifting the focus. Further research on control methods during the droplet jump on the presented microfluidic platform could be interesting.

Droplet evaporation

When a droplet rests on the mesh, it is exposed to the surrounding atmospheric conditions and evaporates. The evaporation time of a $40\,\mu L$ droplet was measured to be 136 min when no ultrasound was applied and 70 min when constantly trapped by focused ultrasound (see Supplementary Material and Fig. S5). Droplet evaporation is an open problem in open-air microfluidics, and Nelson et al. proposed the enclosure of a droplet in a small, pressurized chamber (32). In addition, coating a droplet with hydrophobic powder can act as a barrier, to reduce evaporation (33). Similarly, ionic fluids with low vapor pressures can be used as carriers to prevent evaporation (34). Evaporation can be problematic for DMFs (including our method) under atmospheric conditions without any prevention mechanisms. On the other hand, the controlled increased rate of evaporation that occurs when ultrasound is applied can be useful in experiments involving solvent evaporation.

In summary, our microfluidic platform enable new research avenues in microfluidics because of its superior jumping capability, power, parallelism, and ease of use; and can be applied in laboratory environments, diagnostics, displays and industry.

Materials and methods
Phased array transducer

A 16 × 16 transducer array (256 transducers), developed based on Morales et al. (35) instructions, was used throughout the experiments. The transducers used were Murata MA40S4S (40 kHz). The array was controlled via serial communication (USB FTDI cable with baud rate = 230,400) with MOFSETs (MIC4127 SOIC8) and an FPGA board (ALTERA Core Board CoreEP4CE6). Full details regarding the hardware (SonicSurface) are available in the Instructables by UpnaLab (36). The voltage applied to the PAT was controlled by adjusting the external power supply (RS PRO bench power supply; IPS-303A, 90W).

Acoustic hologram

To manipulate the target objects dynamically, an acoustic hologram is generated to create a focal point at the target position $\mathbf{x_t}$:

$$\phi_t = -\frac{2\pi f_0}{c_0}[d(\mathbf{x_f}, \mathbf{x_t}) - d(0, \mathbf{x_f})], \tag{1}$$

where $f_0 = 40$ kHz and $c_0 = 341\,\mathrm{ms^{-1}}$ are the acoustic frequency and speed of sound in the air, respectively. d is the Euclidean distance between the two points. $\mathbf{x_f} = (x_f, y_f, z_f)$ and $\mathbf{x_t} = (x_t, y_t, z_t)$ denote the focal position and transducer positions, respectively. In the merging experiments, half of the transducers were focused on droplet A and the other half on droplet B:

$$\phi_t = \begin{cases} -\frac{2\pi f_0}{c_0}[d(\mathbf{x_{f_A}}, \mathbf{x_t}) - d(0, \mathbf{x_{f_A}})], & \text{if } t \text{ is even} \\ -\frac{2\pi f_0}{c_0}[d(\mathbf{x_{f_B}}, \mathbf{x_t}) - d(0, \mathbf{x_{f_B}})], & \text{else} \end{cases} \tag{2}$$

where $\mathbf{x_{f_A}}$ and $\mathbf{x_{f_B}}$ are the focal positions of droplets A and B, respectively. In the experiment involving the simultaneous manipulation of four droplets (Movie S5), IBP method, which iteratively determines transducer phases for target field production at control points, was employed. We refer to the details explanation for the IBP on Marzo et al. (24) The codes are available as shown in the data availability section.

Hydrophobic mesh

A mesh (Q-ho Metal Works, part number E9122, stainless steel SUS316, plain weave, mesh count 150) was hydrophobically treated by spraying with Ultra-Ever Dry (UltraTech International, Inc.). First, a bottom coat was applied and dried. When the bottom coating was sufficiently dry, the top coating was applied and dried. The advancing and receding contact angles are $155.7° \pm 1.5°$ and $138.4° \pm 4.4°$, respectively (i.e. the contact angle hysteresis is $17.3° \pm 5.1°$ and see Supplementary Material). The mesh was mounted on top of a 4 mm thick acrylic plate (180 × 180 mm) with a square hole (80 × 80 mm) cut open in the center. For Fig. 5D, the same hydrophobic coating was used. However, a high-rigidity tungsten mesh (Clever Co., Ltd., plain weave, mesh count 150) was used to allow a large working area and minimize reflections from the surface for visibility.

Liquid and its dispense

Deionized water (KOGA Chemical Mfg Co., Ltd.) was used throughout the study unless otherwise stated. Water was dispensed using a syringe pump (Chemyx Fusion 101); Figs. 2, 3, 4, and 5A, B, C, and E, an electronic pipette (A&D Company, MPA-200) was used to dispense the liquid.

Recording devices

The movement of the droplet was captured using a high-speed camera (Photron INFINICAM UC-1) with a Nikon F-to-C Mount Adaptor (Kenko Tokina) and a single-focus lens (Tamron SP AF180mm F/3.5Di). The camera was connected to a PC using a USB C cable and was controlled using Python 3.7. In Figs. 2, 4, and 5A, the frame rate and image resolution were fixed at 1,000 fps and 1,246 × 1,024 pixels, respectively. The frame rate and image resolution are 2,000 fps and 512 × 1,246 pixels, respectively (Fig. 3). The camera was triggered to start recording when commands were sent to the PAT. To capture the images shown in Fig. 5B, C, and E, a Sony α7 (FE 2.8/90 MACRO lens) was used. Fig. 5D was captured using an iPhone 13 Pro.

Image processing and analysis

Image processing was performed using MATLAB R2020a (37). Lens calibration was performed using a checkerbox with the MATLAB Computer Vision Toolbox (ver. 9.2). The pixel-to-mm conversion rate was obtained by placing an object of known size (i.e. a ruler) at the x–z plane (y = 0). The droplet position was analyzed by subtracting the droplet from the background image. The subtracted

portion was then passed onto the *regionprops* function in MATLAB Image Processing Toolbox (ver. 11.1) to identify the droplet centroids. Sequence photographs (Figs. 3 and 5E) were also generated by overlaying the background-subtracted images. The code for replicate analysis is available in the data availability section.

Microscopy

The adsorption of FITC-BSA onto the hydrophobic mesh was observed using an upright confocal laser scanning microscope LSM880 with a Plan-Apochromat 10× objective lens (420640-9900, Carl Zeiss, Oberkochen, Germany). Tile-scan and Z-stack modes were used to scan the entire FITC-BSA-treated area. The tile images were stitched using Carl Zeiss Zen Black software (38). The mesh and FITC-BSA were visualized using reflection and fluorescence microscopy, respectively (40, 39). A 543 nm laser was used to visualize the mesh, and the reflected light was detected. FITC-BSA was excited by a 488 nm laser, and 490–588 nm fluorescence was detected.

Numerical simulation

The numerical simulations in this study were performed using MATLAB R2020a. The codes used to replicate the simulation results fully are presented in the data availability section. The acoustic pressure field shown in Fig. 1B was calculated based on Huygens' principle as follows:

$$p_{in}(\mathbf{x}, \mathbf{x}_t, \phi_t) = \sum_{t=1}^{T} \frac{P_0}{d(\mathbf{x}, \mathbf{x}_t)} D(\eta) e^{j(kd(\mathbf{x}, \mathbf{x}_t) + \phi_t)}, \quad (3)$$

where p_{in} is the sound pressure, transducer number (T) is 256, $D(\eta) = 2J_1(kr\sin\eta)/kr\sin\eta$ denotes the far-field directivity function of piston source, η is the angle between the normal of the transducer and the position $\mathbf{x}$, $k = 2\pi f_0/c_0$ denotes wavenumber, and P_0 denotes transducer power. We report $P_v = 0.221\,\text{Pa}\,\text{V}^{-1}$ at 1 m for Murata MA40S4S, and P_0 is evaluated by multiplying the applied voltage (A_v): $P_0 = A_v P_v$. The acoustic radiation force (ARF) is typically calculated using the method proposed by Gor'kov (41). However, because the PAT contains strong traveling wave components and uses droplet sizes larger than the Rayleigh limit (i.e. $r > 0.1\lambda$), we used the method developed by Andersson & Ahrens to calculate the ARF (43, 42):

$$F_x = \frac{1}{8\rho_0 c_0^2 k^2} \text{Re}\left\{ \sum_{n=0}^{\infty} \sum_{m=-n}^{n} \Psi_n A_{nm} \right.$$
$$\left. \cdot (S_{n,m}S_{n+1,m+1}^* - S_{n,-m}S_{n+1,-m-1}^*) \right\} \quad (4)$$

$$F_y = \frac{1}{8\rho_0 c_0^2 k^2} \text{Im}\left\{ \sum_{n=0}^{\infty} \sum_{m=-n}^{n} \Psi_n A_{nm} \right.$$
$$\left. \cdot (S_{n,m}S_{n+1,m+1}^* + S_{n,-m}S_{n+1,-m-1}^*) \right\}$$

$$F_z = \frac{1}{8\rho_0 c_0^2 k^2} \text{Re}\left\{ \sum_{n=0}^{\infty} \sum_{m=-n}^{n} \Psi_n B_{nm}(S_{n,m}S_{n+1,m}^*) \right\}, \quad (5)$$

where

$$\Psi = 2i(c_n + c_{n+1}^* + 2c_n c_{n+1}^*)$$

$$A_{nm} = \sqrt{(n+m+1)(n+m+2)/((2n+1)(2n+3))}$$

$$B_{nm} = -2\sqrt{(n+m+1)(n-m+1)/((2n+1)(2n+3))}.$$

$$A_{nm} = \sqrt{(n+m+1)(n+m+2)/((2n+1)(2n+3))}, \quad \text{and}$$

$B_{nm} = -2\sqrt{(n+m+1)(n-m+1)/((2n+1)(2n+3))}$. Here, we assume that the target is solid (i.e. the liquid is rigid compared with air) and that it is perfectly spherical.

$$c_n = -\frac{j_n(ka)j'_n(k_p a) - Zj'_n(ka)jn(k_p a)}{h_n(ka)j'_n(k_p a) - Zh'_n(ka)j_n(k_p a)} \quad (6)$$

where $Z = \frac{\rho_p c_p}{\rho_0 c_0}$ is the relative impedance, with subscript 0 and p indicate the medium and sphere, respectively. The asterisk indicates a complex conjugated element. For a water droplet, the density and speed of sound were assumed to be $1,000\,\text{kg}\,\text{m}^{-3}$ and $1,480\,\text{m}\,\text{s}^{-1}$, respectively. Further, j_n and h_n are the spherical Bessel and Hankel functions of the first kind, respectively, and 'indicates the derivative of each function. This method was independently verified and expanded to include the piston source model proposed by Zehnter et al. (44):

$$S_{n,m} = \sum_t 4\pi P_0 e^{(j\phi_t)} D(\eta) i k h_n(kr^t) Y_{nm}^*(\theta^t, \phi^t). \quad (7)$$

Here, Y_{nm} is the spherical harmonic function, which was implemented using the code developed by Javier Montalt Tordera [https://github.com/jmontalt/harmonicY]. (r^t, θ^t, ϕ^t) are in spherical coordinates and calculated from the center of the levitated sphere to the transducer. The center of the sphere was assumed to be the mesh height plus the radius of the droplet (assuming a perfect sphere). Equations 4–5 were evaluated until the relative tolerance was less than 1×10^{-5}. We verified the validity of the numerical simulation described above, and the results are available in the supplementary material and Figs. S1–S4.

Writing paper

A portion of the text in the manuscript was generated with the assistance of artificial intelligence (AI) software, specifically the OpenAI language model ChatGPT (45). The AI was used to provide text completions and modification, which were then reviewed and edited by the authors to ensure accuracy and relevance to the research presented in the paper.

Supplementary material

Supplementary material is available at *PNAS Nexus* online.

Author contributions

Y.K., T.N., Y.O., and T.F. designed the study methodology. Y.K., T.N., S.S., A.M., and I.E. designed and manufactured the experimental apparatus. Y.K. and T.F. contributed to the experimental design. Y.K., S.S., Y.N., and T.Y. collected experimental data. T.F.

developed and conducted the numerical simulations. Y.K. performed image processing, and Y.K., Y.N., T.Y., N.N., T.H., Y.O., and T.F. analyzed and discussed the results. All the authors contributed to the drafting of the manuscript.

Preprints

Data availability

References

1 Fair RB. 2007. Digital microfluidics: is a true lab-on-a-chip possible? *Microfluid Nanofluidics*. 3(3):245–281.

2 Umapathi U, Shin P, Nakagaki K, Leithinger D, Ishii H. 2018. Programmable droplets for interaction. In: Extended Abstracts of the 2018 CHI Conference on Human Factors in Computing Systems. New York (NY): ACM. p. 1–1.

3 Waheed S, *et al.* 2016. 3D printed microfluidic devices: enablers and barriers. *Lab Chip*. 16(11):1993–2013.

4 Zhang Y, Nguyen NT. 2017. Magnetic digital microfluidics—a review. *Lab Chip*. 17(6):994–1008.

5 Jin Y, *et al.* 2022. Electrostatic tweezer for droplet manipulation. *Proc Natl Acad Sci USA*. 119(2):e2105459119.

6 Sun Q, *et al.* 2019. Surface charge printing for programmed droplet transport. *Nat Mater*. 18(9):936–941.

7 Cho SK, Moon H, Kim C-J. 2003 Feb. Creating, transporting, cutting, and merging liquid droplets by electrowetting-based actuation for digital microfluidic circuits. *J Microelectromech Syst*. 12(1):70–80.

8 Tang X, *et al.* 2017. Mechano-regulated surface for manipulating liquid droplets. *Nat Commun*. 8(1):1–10.

9 Yang C, Ning Y, Ku X, Zhuang G, Li G. 2018. Automatic magnetic manipulation of droplets on an open surface using a superhydrophobic electromagnet needle. *Sens Actuators B Chem*. 257:409–418.

10 Chae JB, Lee SJ, Yang J, Chung SK. 2015. 3D electrowetting-on-dielectric actuation. *Sens Actuator A Phys*. 234:331–338.

11 Lee SJ, Lee S, Kang KH. 2012. Droplet jumping by electrowetting and its application to the three-dimensional digital microfluidics. *Appl Phys Lett*. 100(8):081604.

12 Lee SJ, Hong J, Kang KH, Kang IS, Lee SJ. 2014. Electrowetting-induced droplet detachment from hydrophobic surfaces. *Langmuir*. 30(7):1805–1811.

13 Wang Z, *et al.* 2017. Jumping drops on hydrophobic surfaces, controlling energy transfer by timed electric actuation. *Soft Matter*. 13(28):4856–4863.

14 Li W, Tang X, Wang L. 2020. Photopyroelectric microfluidics. *Sci Adv*. 6(38):eabc1693.

15 Yan W, *et al.* 2021. Optically guided pyroelectric manipulation of water droplet on a superhydrophobic surface. *ACS Appl Mater Interfaces*. 13(19):23181–23190.

16 Mi Y, *et al.* 2021. 3D photovoltaic router of water microdroplets aiming at free-space microfluidic transportation. *ACS Appl Mater Interfaces*. 13(37):45018–45032.

17 Chiou PY, Moon H, Toshiyoshi H, Kim C-J, Wu MC. 2003. Light actuation of liquid by optoelectrowetting. *Sens Actuator A Phys*. 104(3):222–228.

18 Ichimura K, Oh S-K, Nakagawa M. 2000. Light-driven motion of liquids on a photoresponsive surface. *Science*. 288(5471):1624–1626.

19 Andrade MAB, Camargo TSA, Marzo A. 2018. Automatic contactless injection, transportation, merging, and ejection of droplets with a multifocal point acoustic levitator. *Rev Sci Instrum*. 89(12):125105.

20 Foresti D, Nabavi M, Klingauf M, Ferrari A, Poulikakos D. 2013. Acoustophoretic contactless transport and handling of matter in air. *Proc Natl Acad Sci USA*. 110(31):12549–12554.

21 Vasileiou T, Foresti D, Bayram A, Poulikakos D, Ferrari A. 2016. Toward contactless biology: acoustophoretic DNA transfection. *Sci Rep*. 6(1):20023.

22 Watanabe A, Hasegawa K, Abe Y. 2018. Contactless fluid manipulation in air: droplet coalescence and active mixing by acoustic levitation. *Sci Rep*. 8(1):10221.

23 Marzo A, *et al.* 2015 Oct. Holographic acoustic elements for manipulation of levitated objects. *Nat Commun*. 6(1):8661.

24 Marzo A, Drinkwater BW. 2018. Holographic acoustic tweezers. *Proc Natl Acad Sci USA*. 116(1):84–89.

25 Nguyen T-V, *et al.* 2021. Direct measurement of impacting force between a droplet and a superhydrophobic blade. In: 2021 IEEE 34th International Conference on Micro Electro Mechanical Systems (MEMS). Gainesville, FL, USA: IEEE. p. 771–774.

26 Ando Y, Homma Y, Hiruta Y, Citterio D, Suzuki K. 2009. Structural characteristics and optical properties of a series of solvatochromic fluorescent dyes displaying long-wavelength emission. *Dyes Pigm*. 83(2):198–206.

27 Pan S, Kota AK, Mabry JM, Tuteja A. 2013. Superomniphobic surfaces for effective chemical shielding. *J Am Chem Soc*. 135(2):578–581.

28 Au SH, Kumar P, Wheeler AR. 2011. A new angle on pluronic additives: advancing droplets and understanding in digital microfluidics. *Langmuir*. 27(13):8586–8594.

29 Luk VN, Mo GCH, Wheeler AR. 2008. Pluronic additives: a solution to sticky problems in digital microfluidics. *Langmuir*. 24(12):6382–6389.

30 Srinivasan V, Pamula VK, Fair RB. 2004. An integrated digital microfluidic lab-on-a-chip for clinical diagnostics on human physiological fluids. *Lab Chip*. 4(4):310–315.

31 Yoon JY, Garrell RL. 2003. Preventing biomolecular adsorption in electrowetting-based biofluidic chips. *Anal Chem*. 75(19):5097–5102.

32 Nelson WC, Yen M, Keng PY, Van Dam RM, Kim C-J. 2011. High pressure EWOD digital microfluidics. In: 2011 16th International Solid-State Sensors, Actuators and Microsystems Conference. Beijing, China: IEEE. p. 2932–2935.

33 Tosun A, Erbil HY. 2009. Evaporation rate of PTFE liquid marbles. *Appl Surf Sci*. 256(5):1278–1283.

34 Dubois P, *et al.* 2006. Ionic liquid droplet as e-microreactor. *Anal Chem*. 78(14):4909–4917.

35 Morales R, Ezcurdia I, Irisarri J, Andrade MAB, Marzo A. 2021. Generating airborne ultrasonic amplitude patterns using an open hardware phased array. *Appl Sci*. 11(7):2981.

36 UpnaLab. 2023. Sonicsurface: phased-array for levitation, mid-air tactile feedback and target directional speakers. https://www.instructables.com/SonicSurface-Phased-array-for-Levitation-Mid-air-T/.

37 Mathworks. Matlab. https://jp.mathworks.com/.

38 Zeiss C. Zen. https://www.zeiss.co.jp/microscopy/products/microscope-software/zen.html.

39 Inaba T, *et al.* 2013. Three-dimensional visualization of mixed species biofilm formation together with its substratum. *Microbiol Immunol*. 57(8):589–593.

40 Yawata Y, *et al.* 2010. Monitoring biofilm development in a micro-fluidic device using modified confocal reflection microscopy. *J Biosci Bioeng.* 110(3):377–380.

41 Gor'kov LP. 1962. On the forces acting on a small particle in an acoustical field in an ideal fluid. *Soviet Dokl Phys.* 6:773–775.

42 Andersson C. 2022. Acoustic levitation of multi-wavelength spherical bodies using transducer arrays of non-specialized geometries. *J Acoust Soc Am.* 151(5):2999–3006.

43 Andersson C, Ahrens J. 2019. Acoustic levitation from superposition of spherical harmonics expansions of elementary sources: analysis of dependency on wavenumber and order. In: 2019 IEEE International Ultrasonics Symposium (IUS). Glasgow, UK: IEEE. p. 920–923.

44 Zehnter S, Andrade MAB, Ament C. 2021. Acoustic levitation of a Mie sphere using a 2D transducer array. *J Appl Phys.* 129(13):134901.

45 OpenAI. 2023. Chatgpt. https://openai.com/chatgpt.